Exact Non–Reflecting Boundary Conditions on General Domains and *hp*–Finite Elements

Tommy L. Binford, Jr. [a], David P. Nicholls [b,*], Nilima Nigam [c], Tim Warburton [a]

[a] *Computational and Applied Mathematics, Rice University, Houston, Texas 77005*

[b] *Department of Mathematics, Statistics, and Computer Science, University of Illinois at Chicago, Chicago, IL 60607*

[c] *Department of Mathematics and Statistics, McGill University, Montréal, QC, H3A 2K6, Canada*

Abstract

The scattering of time–harmonic electromagnetic and linear acoustic waves from a bounded obstacle arises in a wide array of applications. Despite the linear nature of the governing partial differential equations, the unboundedness of the problem domain presents a particular difficulty for numerical simulations. In many situations an integral equation method can be readily applied, however, in some applications, e.g. inhomogeneous obstacles, a volumetric discretization is required and Finite Element Methods (FEM) are particularly appealing due to their geometric flexibility, reliability, and the widespread availability. In such situations one introduces an Artificial Boundary to truncate the unbounded exterior domain to one of finite extent, and enforces a Non–Reflecting Boundary Condition there. Classical approaches require that the shape of this boundary must be quite specific, circular or elliptical, so that an exact Dirichlet–to–Neumann (DtN) map can be computed to enforce the boundary condition. This method (the DtN–FE method) suffers from two important flaws: The non–local nature of the DtN map, and the very specific shape requirements for the artificial boundary. In a sequence of recent papers, two of the authors have addressed the latter of these concerns with a generalization of the DtN–FE method. This "Enhanced DtN–FE" method permits Artificial Boundaries which are shaped as perturbations of a circle, and is based upon the fact that the DtN map depends analytically upon shape perturbation. In this paper we extend this method to a two–dimensional FEM featuring high–order polynomials in order to realize a greater rate of convergence. This is more involved than simply specifying high–order test and trial functions as now the scatterer shapes and Artificial Boundary must be faithfully represented. This entails boundary elements which conform (to high order) to the true boundary shapes. As we show, this can be accomplished and we realize an arbitrary order FEM without spurious reflections.

Key words: Non–reflecting boundary conditions, *hp*–finite elements, acoustic

scattering, electromagnetic scattering, Dirichlet–to–Neumann maps, geometric perturbation methods.

1 Introduction

The scattering of time–harmonic electromagnetic and linear acoustic waves from a bounded obstacle arises in a wide array of applications of great importance to scientists and engineers. Such applications include remote sensing, radar imaging, and non–destructive testing. Despite the linear nature of the governing partial differential equations, several inherent features of these applications give rise to many difficult algorithmic and theoretical challenges. Among these is the fundamentally unbounded nature of the problem domain which presents a particular difficulty for numerical simulations.

In many situations an integral equation method can be readily applied in the frequency domain [1] which not only posits near–field unknowns, but also satisfies the far–field condition, the "Sommerfeld Radiation Condition," exactly via an astute choice of integral kernel. However, some applications, such as an inhomogeneous obstacle with a discontinuous index of refraction, require a *volumetric* discretization; here Finite Element Methods (FEM) are particularly appealing due to their geometric flexibility, reliability, and the widespread availability of FEM software. In a volumetric discretization an Artificial Boundary is typically introduced to the computational domain (exterior to the scatterer) to render it bounded, and an approximation of the Sommerfeld Radiation Condition [1] is enforced there. There is a large literature of such methods and we refer the interested reader to the excellent survey book of Ihlenburg [2].

Of particular relevance to the present paper is the work in the frequency domain of Feng [3], Han & Wu [4], and Keller, & Givoli [5–9] (please see [2] for a complete literature survey). In these the shape of the Artificial Boundary must be chosen to be quite simple: Circular or elliptical (spherical or ellipsoidal in three dimensions), i.e. a separable geometry. In this case the solution exterior to the Artificial Boundary can be written *exactly* in terms of appropriate basis functions (e.g. Hankel functions), which can then be used to readily compute the Dirichlet–to–Neumann map (DtN map) enabling a "Non–Reflecting" (or "Transparent") boundary condition to be posed at the Artificial Boundary.

* Corresponding author.
Email addresses: tbinford@caam.rice.edu (Tommy L. Binford, Jr.), nicholls@math.uic.edu (David P. Nicholls), nigam@math.mcgill.ca (Nilima Nigam), timwar@caam.rice.edu (Tim Warburton).

An FEM linked to the Non–Reflecting boundary condition, featuring the DtN map, results in the DtN–FE method. This method, however, suffers from two important flaws: The non–local nature of the DtN map, and the very specific shape requirements for the Artificial Boundary. The first results in the appearance of dense sub–blocks in the otherwise sparse linear system of equations which must be solved. The second results in a needlessly large computational domain if the scatterer cannot be efficiently enclosed by a circle or ellipse.

In a sequence of recent papers, two of the authors have addressed the latter of these concerns with a generalization of the DtN–FE method [10,11]. This "Enhanced DtN–FE" method permits Artificial Boundaries which are shaped as *perturbations* of a circle, and is based upon the fact that the DtN map depends *analytically* upon shape perturbation. With the wide range of shapes that one can specify in this way, this generalization allows one to fit the Artificial Boundary quite close to the surface of the scatterer. In the paper [10] it was demonstrated that this method can be implemented and coupled to a piecewise linear FEM while not destroying its inherent convergence rate. In this paper we extend this method to a two–dimensional FEM featuring high–order polynomials in order to realize a higher rate of convergence. This is more involved than simply specifying test and trial functions of higher polynomial order as now the scatterer shapes *and* Artificial Boundary must be faithfully represented, i.e. the boundary elements must conform (to high order) to the true boundary shapes. However, as we shall see in the numerical results of § 5, this can be accomplished and we realize an arbitrary order FEM without spurious reflections.

The organization of the paper is as follows: In § 2 we review the governing equations of time–harmonic acoustic and electromagnetic scattering by a bounded obstacle in the frequency domain. In § 3 we specify the details of our *hp*–FEM including the particulars of accommodating curved boundaries. In § 4 we recall the considerations necessary to compute the DtN map for use in our new FEM scheme, and in § 5 we present a representative set of numerical examples which display the accuracy, flexibility, and robustness of our new high–order, Enhanced DtN–FE method. Concluding remarks are given in § 6.

2 Governing Equations

It is well–known [1] that if time–harmonic plane–wave acoustic or electromagnetic radiation of the form

$$v_i = e^{ik\alpha\cdot x}, \quad |\alpha| = 1, \tag{1}$$

is incident upon a bounded, impenetrable (perfectly conducting) obstacle $\Sigma \subset \mathbf{R}^2$ (with boundary Γ) then the (reduced) scattered field $v = v(r, \theta)$ satisfies the scalar Helmholtz equation

$$\Delta v + k^2 v = 0 \qquad \text{in } \Omega_\infty := \text{Ext}(\Sigma). \tag{2}$$

Of course, to realize a unique solution one must specify, in addition to the periodicity in θ, boundary conditions at the scatterer and at infinity. For the former, we choose a Dirichlet condition

$$v|_\Gamma = -\, v_i|_\Gamma =: \xi(\theta), \tag{3}$$

which defines the generic Dirichlet data ξ (a Neumann condition can be treated in an analogous manner). For the latter, we have the Sommerfeld Radiation Condition [1] (in two dimensions):

$$\lim_{r\to\infty} r^{1/2}(\partial_r v - ikv) = 0. \tag{4}$$

Gathering (2), (3), and (4) we have the equations governing the scattering of time–harmonic, acoustic or electromagnetics plane–waves from an irregular, impenetrable, two–dimensional obstacle:

$$\Delta v + k^2 v = 0 \qquad \text{in } \Omega_\infty \tag{5a}$$
$$v|_\Gamma = \xi \tag{5b}$$
$$\lim_{r\to\infty} r^{1/2}(\partial_r v - ikv) = 0. \tag{5c}$$

2.1 A Transparent Boundary Condition

One of the severe difficulties associated with the numerical simulation of the system (5) is the unbounded nature of the computational domain, Ω_∞. In FEM discretizations (as with other volumetric techniques) this problem is usually addressed with the introduction of an "Artificial Boundary," say $\mathcal{B}$, which *properly* encloses the scatterer Σ, and the imposition there of some boundary conditions motivated by the Sommerfeld Radiation Condition (4). We now describe a "transparent" or "non–reflecting" boundary condition which can be enforced on such an Artificial Boundary. For this, consider the augmented

scattering problem

$$\Delta v + k^2 v = 0 \qquad \text{in } \Omega := \Omega_\infty \backslash \mathrm{Ext}(\mathcal{B}) \tag{6a}$$
$$v = \xi \qquad \text{at } \Gamma \tag{6b}$$
$$\partial_N v = \partial_N w \qquad \text{at } \mathcal{B} \tag{6c}$$
$$v = w \qquad \text{at } \mathcal{B} \tag{6d}$$
$$\Delta w + k^2 w = 0 \qquad \text{in } \mathrm{Ext}(\mathcal{B}) \tag{6e}$$
$$\lim_{r\to\infty} r^{1/2}(\partial_r w - ikw) = 0, \tag{6f}$$

where N is a normal pointing into the *interior* of $\mathcal{B}$; please see Figure 1. The

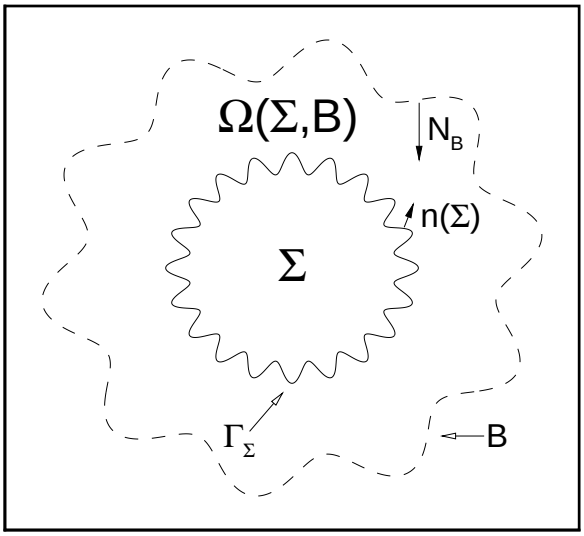

Fig. 1. Depiction of a scatterer, Σ, with boundary Γ and unit exterior normal n enclosed within the artificial boundary $\mathcal{B}$ with normal $N_\mathcal{B}$. The region $\Omega(\Sigma, \mathcal{B})$ is the intersection of the exterior of Σ with the interior of $\mathcal{B}$.

solutions of (5) and (6) are identical in that the v match on Ω, and $v = w$ on the exterior of $\mathcal{B}$.

To specify the transparent boundary condition on v at $\mathcal{B}$ consider (6d)–(6f):

$$\Delta w + k^2 w = 0 \qquad \text{in } \mathrm{Ext}(\mathcal{B}) \tag{7a}$$
$$w = \psi \qquad \text{at } \mathcal{B} \tag{7b}$$
$$\lim_{r\to\infty} r^{1/2}(\partial_r w - ikw) = 0, \tag{7c}$$

where ψ is meant to denote generic Dirichlet data at $\mathcal{B}$. Provided that $\mathcal{B}$ is sufficiently regular and ψ sits in an appropriate function space (see, e.g., [1]), this system of equations has a unique solution. From this we can compute

the quantity necessary to close (6a)–(6c), $\partial_N w$ at $\mathcal{B}$, i.e. the "Dirichlet–to–Neumann map" (DtN map)

$$T(\mathcal{B})[\psi] := \nabla w|_{\mathcal{B}} \cdot N. \tag{8}$$

We point out that this map is also known as the Dirichlet–Neumann operator and the Stekhlov–Poincaré map. In § 4 we will make a particular choice of N which has adjointness properties (see § A) which allow one to accelerate one of the algorithms we describe (Operator Expansions) to compute T (see § 4.2).

Therefore, based upon the augmented system (6), we can equivalently restate (5) on the *bounded* domain Ω

$$\Delta v + k^2 v = 0 \qquad \text{in } \Omega \tag{9a}$$
$$v = \xi \qquad \text{at } \Gamma \tag{9b}$$
$$\partial_N v - T[v] = 0 \qquad \text{at } \mathcal{B}, \tag{9c}$$

with the transparent boundary condition at $\mathcal{B}$ is specified via the non–local DtN map, T. In § 3 we describe a method for discretizing (9) using high–order *hp*–Finite Elements, and in § 4 we elucidate two "Boundary Perturbation" procedures for computing the DtN map, T. Finally, in § 5 we display an array of numerical examples which exhibit the flexibility, reliability, and accuracy one can achieve with this new method.

3 *p*–Type Modal Finite Elements

In previous work [10], two of the authors investigated an algorithm which coupled an efficient implementation of the DtN map, T, to a volumetric Finite Element discretization of (9) on Ω. In that work, we used piecewise linear basis and test functions on triangles so that our approximate solution was a piecewise linear polynomial. The current work extends this idea to couple the DtN map to a continuous *p*–Finite Element method. The basis functions employed are sometimes referred to as *modal bases* [12,13], and we briefly describe them here.

To begin, we subdivide the bounded region Ω using into K triangles; the triangles at the Artificial Boundary $\mathcal{B}$ are mapped isoparametrically to fit the curve, i.e.

$$\Omega = \bigcup_{k=1}^{K} \Omega^k.$$

Continuous functions on Ω are now approximated by

$$f(x,y) = \sum_{k=1}^{K} \sum_{n=1}^{N} f_n^k \phi_n^k(a,b)$$

where the f_n^k are the expansion coefficients. The coordinates $a = a(x, y)$ and $b = b(x, y)$ are the variables in which integration and differentiation are performed, and are chosen [13] to transform the triangles Ω^k to the reference square $\{(a, b) \mid -1 \leq a, b \leq 1\}$. The introduction of these new coordinates allows, for instance, L^2–inner products of basis functions on Ω_k to be computed tensorially as

$$(f, g) = \int_{\Omega_k} f(x, y)\overline{g(x, y)}\, dx\, dy = \int_{-1}^{1}\int_{-1}^{1} f(a, b)\overline{g(a, b)}J_{a,b}\, da\, db,$$

where $J_{a,b}$ is the Jacobian of the transformation. For these integrations we use highly accurate Gauss–Lobatto–Legendre and Gauss–Radau–Jacobi quadratures.

The finite element basis functions ϕ_n^k are further chosen so as to reduce the number of computations involved per quadrature. Our basis consists of interior and boundary modes, the former vanish on element boundaries. Global continuity is thus enforced by ensuring continuity of boundary modes. The one–dimensional shape functions are constructed to have unit value along one edge of the triangulation while being zero at all other edges. The interior modes are carefully chosen Jacobi polynomials.

In order to implement the combined DtN–FE method, we follow the standard procedure and begin by multiplying (9a) by a test function, ϕ_n^k and integrate over Ω. Since we have Dirichlet data on the inner boundary, we obtain the following variational formulation of the problem: *Find* $v \in \{w \in H^1(\Omega) \mid w|_\Gamma = \xi\}$ *such that*

$$(\nabla v, \nabla\phi_k^n) - k^2(v, \phi_k^n) + \int_{\mathcal{B}} T[v]\overline{\phi_n^k}\, ds = 0, \qquad \forall\phi_n^k \in \{w \in H^1(\Omega) \mid w|_\Gamma = 0\}.$$

As a final note, we point out that instead of adaptively investigating refinements in polynomial order p and mesh–size h simultaneously, we fix a polynomial order, and then refine the mesh. This allowed us to assess the effects of using the DtN maps with both h and p refinements separately. Quadrature errors in this framework are small.

4 The Dirichlet–to–Neumann Map

In order to completely specify the numerical method presented in § 3 we must compute the DtN map, T, at the Artificial Boundary $\mathcal{B}$. The case of a circular boundary

$$\mathcal{B} = \{r = b\}$$

has been investigated by Feng [3], Han & Wu [4], and Keller, & Givoli [5–9]. In this case the *exact* solution of (7) is:

$$w(r,\theta) = \sum_{p=-\infty}^{\infty} \frac{H_p^{(1)}(kr)}{H_p^{(1)}(kb)} \hat{\psi}_p e^{ip\theta},$$

where $\hat{\psi}_p$ is the p–th Fourier coefficient of ψ and $H_p^{(1)}$ is the p–th Hankel function of the first kind. From (8) the DNO is

$$T(r=b)[\psi] = -\sum_{p=-\infty}^{\infty} bk \frac{d_z H_p^{(1)}(kb)}{H_p^{(1)}(kb)} \hat{\psi}_p e^{ip\theta} = -kb \frac{d_z H_D^{(1)}(kb)}{H_D^{(1)}(kb)} [\psi] \tag{10}$$

where d_z is differentiation with respect the argument of the Hankel function, and we have identified the Fourier multiplier $m(D)$:

$$m(D)[\psi] := \sum_{p=-\infty}^{\infty} m(p) \hat{\psi}_p e^{ip\theta}.$$

This method was significantly expanded in [10] to include Artificial Boundaries of the form

$$\mathcal{B} = \{r = b + g(\theta)\}, \tag{11}$$

i.e. perturbations of a circle. This generalization is significant as it allows the construction of Artificial Boundaries which are close to the surface of the scatterer, resulting in a computational domain, Ω, with a quite modest number of elements. We will see evidence of this in § 5 and show the remarkable gains that can be achieved over the original DtN–FE method with an appropriate choice of $\mathcal{B}$.

Of course the difficult task that remains is the computation of the DtN map on a domain with the general shape, (11). In fact, the form of our new class of Artificial Boundaries suggests that a perturbative method should be both convenient and highly accurate. To make this clearer, if we specify $g = \varepsilon f$, it can be shown [10] that both the field, $w = w(x, y; \varepsilon)$, and the DNO, $T = T(\varepsilon f)$, depend analytically upon ε and that the expansions:

$$w(x,y;\varepsilon) = \sum_{n=0}^{\infty} w_n(x,y)\varepsilon^n, \quad T(\varepsilon f)[\psi] = \sum_{n=0}^{\infty} T_n(f)[\psi]\varepsilon^n, \tag{12}$$

are *strongly* convergent in an appropriate Sobolev space. Clearly, a truncation of the Taylor series for the DtN map,

$$T^N(\varepsilon f)[\psi] := \sum_{n=0}^{N} T_n(f)[\psi]\varepsilon^n \tag{13}$$

should prove to be a highly accurate approximation to T, and will be very convenient if a good formula for the T_n can be identified. For this purpose

several "Boundary Perturbation" techniques have been developed, and in the following two sections we describe two methods which are both fast and accurate.

4.1 Field Expansions

The method of "Field Expansions" (FE) for computational scattering can be traced back to the pioneering work of Rayleigh [14] and Rice [15], and was extended to a reliable high–order method by Bruno & Reitich [16–21]. This FE method is based upon the analyticity properties of w and T, see (12), and recursion formulas for the w_n and T_n which can be realized with the following calculations for the case $\mathcal{B} = \{r = b+\varepsilon f\}$. We begin by inserting the expansion for w, (12), into (7) and realizing that the w_n must satisfy

$$\Delta w_n + k^2 w_n = 0 \qquad r > b, \tag{14a}$$

$$w_n(b,\theta) = \delta_{n,0}\psi - \sum_{l=0}^{n-1} \frac{f^{n-l}}{(n-l)!}\partial_r^{n-l} w_l(b,\theta), \tag{14b}$$

$$\lim_{r\to\infty} r^{1/2}(\partial_r w_n - ikw_n) = 0, \tag{14c}$$

where $\delta_{n,m}$ is the Kronecker delta. The solution of (14a) & (14c) is

$$w_n(r,\theta) = \sum_{p=-\infty}^{\infty} d_{p,n} \frac{H_p^{(1)}(kr)}{H_p^{(1)}(kb)} e^{ip\theta}.$$

Equation (14b) can be used to solve for $d_{p,n}$:

$$d_{p,n} = \delta_{n,0}\hat{\psi}_p - \sum_{l=0}^{n-1}\sum_{q=-\infty}^{\infty} C_{p-q,n-l} \frac{d_z^{n-l} H_p^{(1)}(kb)}{H_p^{(1)}(kb)} d_{q,l},$$

where

$$C_l(\theta) := \frac{k^l f^l(\theta)}{l!}, \quad C_l(\theta) =: \sum_{p=-\infty}^{\infty} C_{l,p} e^{ip\theta}.$$

Given the $d_{p,n}$ we can now compute the n–th term of the DtN map. At this point we define

$$N_g := (-(b+g), \partial_\theta g)^T$$

as our normal vector which will produce a DtN map with advantageous adjointness properties (see § 4.2 & § A). Recalling (8) & (12), and that $\nabla =$

$(\partial_r, (1/r)\partial_\theta)^T$,

$$\begin{aligned} T(\varepsilon f)[\psi] &= \nabla w(b+\varepsilon f(\theta),\theta)\cdot N_{\varepsilon f} \\ &= \sum_{n=0}^{\infty}\sum_{p=-\infty}^{\infty}\left[-k(b+\varepsilon f)\frac{d_z H_p^{(1)}(k(b+\varepsilon f))}{H_p^{(1)}(kb)}\right. \\ &\quad \left. + \frac{\varepsilon\partial_\theta f}{(b+\varepsilon f)}(ip)\frac{H_p^{(1)}(k(b+\varepsilon f))}{H_p^{(1)}(kb)}\right] d_{p,n}e^{ip\theta}\varepsilon^n. \end{aligned}$$

A recursion for the $T_n(f)$ can be realized by multiplying by $(b+\varepsilon f)$ (to remove quotients involving ε), and expanding the DtN map in powers of ε:

$$\begin{aligned} T_n(f)[\psi] &= -kb\sum_{l=0}^{n}\sum_{p=-\infty}^{\infty}\frac{(kf)^{n-l}}{(n-l)!}\frac{d_z^{n+1-l}H_p^{(1)}(kb)}{H_p^{(1)}(kb)}d_{p,l}e^{ip\theta} \\ &\quad - \frac{f}{b}T_{n-1}(f)[\psi] \\ &\quad - 2kf\sum_{l=0}^{n-1}\sum_{p=-\infty}^{\infty}\frac{(kf)^{n-1-l}}{(n-1-l)!}\frac{d_z^{n-l}H_p^{(1)}(kb)}{H_p^{(1)}(kb)}d_{p,l}e^{ip\theta} \\ &\quad - \frac{k}{b}f^2\sum_{l=0}^{n-2}\sum_{p=-\infty}^{\infty}\frac{(kf)^{n-2-l}}{(n-2-l)!}\frac{d_z^{n-1-l}H_p^{(1)}(kb)}{H_p^{(1)}(kb)}d_{p,l}e^{ip\theta} \\ &\quad + \frac{1}{b}(\partial_\theta f)\sum_{l=0}^{n-1}\sum_{p=-\infty}^{\infty}\frac{(kf)^{n-1-l}}{(n-1-l)!}\frac{d_z^{n-1-l}H_p^{(1)}(kb)}{H_p^{(1)}(kb)}(ip)d_{p,l}e^{ip\theta}, \end{aligned} \tag{15}$$

or,

$$\begin{aligned} T_n(f)[\psi] &= -kb\sum_{l=0}^{n}C_{n-l}\frac{d_z^{n+1-l}H_D^{(1)}(kb)}{H_D^{(1)}(kb)}\mathcal{D}_l \\ &\quad - \frac{f}{b}T_{n-1}(f)[\psi] \\ &\quad - 2kf\sum_{l=0}^{n-1}C_{n-1-l}\frac{d_z^{n-l}H_D^{(1)}(kb)}{H_D^{(1)}(kb)}\mathcal{D}_l \\ &\quad - \frac{k}{b}f^2\sum_{l=0}^{n-2}C_{n-2-l}\frac{d_z^{n-1-l}H_D^{(1)}(kb)}{H_p^{(1)}(kb)}\mathcal{D}_l \\ &\quad + \frac{1}{b}(\partial_\theta f)\sum_{l=0}^{n-1}C_{n-1-l}\frac{d_z^{n-1-l}H_D^{(1)}(kb)}{H_D^{(1)}(kb)}\partial_\theta\mathcal{D}_l, \end{aligned} \tag{16}$$

where

$$\mathcal{D}_l(\theta) := \sum_{p=-\infty}^{\infty} d_{p,l}e^{ip\theta}.$$

Once these are computed, the approximation T^N, c.f. (13), of T can be implemented.

A second approach to the numerical simulation of DtN maps, in the setting of acoustic and electromagnetic scattering, is due to Milder [22–27]. In this "Operator Expansions" (OE) method one works exclusively with the operator, T, and, using the analyticity properties of the DNO and the expansion (12), this method computes the T_n *directly*. We begin by noting that a solution of (7a) & (7c) is

$$w_p(r,\theta) = H_p^{(1)}(kr)e^{ip\theta}.$$

Since

$$\psi_p(\theta) = w_p(b+\varepsilon f,\theta) = H_p^{(1)}(k(b+\varepsilon f))e^{ip\theta}$$

the definition of the DtN map, (8), yields

$$\begin{aligned} T(\varepsilon f)\left[H_p^{(1)}(k(b+\varepsilon f))e^{ip\theta}\right] &= -(b+\varepsilon f)\partial_r\left(H_p^{(1)}(kr)e^{ip\theta}\right)\Big|_{r=b+\varepsilon f} \\ &\quad + \frac{\varepsilon\partial_\theta f}{b+\varepsilon f}\partial_\theta\left(H_p^{(1)}(kr)e^{ip\theta}\right)\Big|_{r=b+\varepsilon f}, \end{aligned}$$

that is

$$\begin{aligned} T(\varepsilon f)\left[H_p^{(1)}(k(b+\varepsilon f))e^{ip\theta}\right] &= -k(b+\varepsilon f)d_z H_p^{(1)}(k(b+\varepsilon f))e^{ip\theta} \\ &\quad + \frac{\varepsilon\partial_\theta f}{b+\varepsilon f}(ip)H_p^{(1)}(k(b+\varepsilon f))e^{ip\theta}. \quad (17) \end{aligned}$$

Expanding in powers of ε and recognizing $(b+\varepsilon f)^{-1}$ as a geometric series,

$$\begin{aligned} &\left(\sum_{n=0}^{\infty} T_n(f)\ \varepsilon^n\right)\left[\sum_{n=0}^{\infty} d_z^n H_p^{(1)}(kb)\frac{k^n f^n}{n!}e^{ip\theta}\varepsilon^n\right] \\ &\qquad = -kb\sum_{n=0}^{\infty} d_z^{n+1} H_p^{(1)}(kb)\frac{k^n f^n}{n!}e^{ip\theta}\varepsilon^n \\ &\qquad\quad - k(\varepsilon f)\sum_{n=0}^{\infty} d_z^{n+1} H_p^{(1)}(kb)\frac{k^n f^n}{n!}e^{ip\theta}\varepsilon^n \\ &\quad + \varepsilon(\partial_\theta f)\left(\frac{1}{b}\sum_{n=0}^{\infty}\left(\frac{-f}{b}\right)^n\varepsilon^n\right)(ip)\left(\sum_{n=0}^{\infty} d_z^n H_p^{(1)}(kb)\frac{k^n f^n}{n!}e^{ip\theta}\varepsilon^n\right). \quad (18) \end{aligned}$$

At order ε^0 we find

$$T_0[H_p^{(1)}(kb)e^{ip\theta}] = -kb\ d_z H_p^{(1)}(kb)e^{ip\theta},$$

which simplifies to

$$T_0[e^{ip\theta}] = -kb\frac{d_z H_p^{(1)}(kb)}{H_p^{(1)}(kb)}e^{ip\theta}.$$

Since any periodic function $\psi(x)$ can be expressed as a linear combination of complex exponentials $\exp(ip\theta)$ through their Fourier series, we can conclude

that

$$T_0[\psi] = -kb\frac{d_z H_D^{(1)}(kb)}{H_D^{(1)}(kb)}[\psi],$$

which, of course, coincides with (10).

At order n (18) yields, recalling that $C_n = k^n f^n/n!$,

$$\begin{aligned} T_n(f)\left[e^{ip\theta}\right] = &-kbC_n\frac{d_z^{n+1}H_p^{(1)}(kb)}{H_p^{(1)}(kb)}e^{ip\theta} - kfC_{n-1}\frac{d_z^n H_p^{(1)}(kb)}{H_p^{(1)}(kb)}e^{ip\theta} \\ &+ (\partial_\theta f)\sum_{l=0}^{n-1} C_l\frac{1}{b}\left(\frac{-f}{b}\right)^l (ip)\frac{d_z^{n-l-1}H_p^{(1)}(kb)}{H_p^{(1)}(kb)}e^{ip\theta} \\ &- \sum_{l=0}^{n-1} T_l(f)\left[C_{n-l}\frac{d_z^{n-l}H_p^{(1)}(kb)}{H_p^{(1)}(kb)}e^{ip\theta}\right]. \end{aligned}$$

Again, recognizing ψ as a sum of Fourier modes, $e^{ip\theta}$, and identifying factors such as (ip) with operators ∂_θ, we write

$$\begin{aligned} T_n(f)[\psi] = &-bkC_n\frac{d_z^{n+1}H_D^{(1)}(kb)}{H_D^{(1)}(kb)}[\psi] - kfC_{n-1}\frac{d_z^n H_D^{(1)}(kb)}{H_D^{(1)}(kb)}[\psi] \\ &+ \sum_{l=0}^{n-1} C_{n-1-l}\frac{(\partial_\theta f)(-1)^l f^l}{b^{l+1}}\partial_\theta\frac{d_z^{n-1-l}H_D^{(1)}(kb)}{H_D^{(1)}(kb)}[\psi] \\ &- \sum_{l=0}^{n-1} T_l(f)\left[C_{n-l}\frac{d_z^{n-l}H_D^{(1)}(kb)}{H_D^{(1)}(kb)}[\psi]\right]. \end{aligned} \tag{19}$$

At this point a careful accounting of the computational complexity of this OE algorithm is in order. As a preliminary step, the powers of $C_l = k^l f^l/l!$ can be computed in $\mathcal{O}(lN_x\log(N_x))$ if N_x Fourier coefficients for f are retained. However, an inspection of the final term in (19) reveals that, given a fixed ψ, the cost of this algorithm grows *factorially* in n as T_l must be *recomputed* on a different argument n–many times at each order. This clearly compares very unfavorably with the $\mathcal{O}(n^2N_x\log(N_x))$ cost of the FE algorithm. However, we show in § A that the adjointness properties of T can be used to compute the term T_n in $\mathcal{O}(nN_x\log(N_x))$ yielding an overall cost identical to the FE method.

5 Numerical Results

In this section we present the results of some numerical experiments which illustrate the flexibility and applicability of our new algorithm. Among the

wide array of possible computations we could attempt we have chosen three which are representative of the capabilities of our approach: Scattering from a cylinder, scattering from an ellipse, and scattering from a "star–shaped" obstacle. The first is chosen as we can appeal to an exact solution which will validate our numerical simulations, the second is a non–trivial generalization of the first, while the third demonstrates quite effectively how our new approach can enable huge computational savings with a well–chosen artificial boundary.

To give an idea of the performance of our numerical scheme we have selected, for all of the simulations given below, two sample frequencies:

$$k_1 = 60\pi/180 \approx 1.04719, \quad k_2 = 600\pi/180 \approx 10.4719.$$

These are simply two rather low–frequency values of k which avoid any numerical resonances [11]. For convenience of presentation these are listed below as $k \approx 1$ and $k \approx 10$.

5.1 Scattering from a Cylinder

To begin we consider radiation incident upon a perfectly conducting scatterer shaped by a circle of radius one so that

$$\Sigma_c = \{r < a\}, \quad \Gamma_c = \{r = a\}, \quad a = 1,$$

c.f. § 2. This obstacle can be efficiently enclosed by a transparent boundary of circular shape with radius b,

$$\mathcal{B} = \{r = b\}.$$

With this choice, we recover the DtN–FE method of Feng [3], Han & Wu [4], and Keller, & Givoli [5]. However, in all of these implementations only a piecewise linear FEM was utilized. For the first time we present numerical results of this DtN–FE method coupled to a high–order *hp*–FEM. A convenient feature of this particular numerical example is the existence of an exact solution [1] for this configuration which we utilize in simulations presented below. The numerical parameters for the circular scatterer simulations are summarized in Tables 1 ($b = 2$) & 6 ($b = 1.2$). As there is no perturbation of the Artificial Boundary we obtain an *exact* boundary condition at $\mathcal{B}$ with $N = 0$ terms in the expansion of the DNO; furthermore, both the OE and FE algorithms deliver the same expression.

In Tables 2–5 ($b = 2$) and 7–10 ($b = 1.2$) we present the results of our numerical simulations as compared to the exact solution. In these we notice several things, first, our new boundary condition *never* interferes with the performance of the underlying FEM. To make this more precise we compute, in

columns 4 & 7 of the Tables,

$$\text{ratio} := \text{ratio}(h_{n-1}, h_n) = \frac{\left|u_{exact} - u_{h_{n-1}}\right|_{L^\infty}}{\left|u_{exact} - u_{h_n}\right|_{L^\infty}},$$

where u_{exact} is the exact solution and u_{h_n} is the numerical solution at refinement level h_n. This quantity is the incremental L^∞–error reduction factor from one refinement to the next, and we find that it is always within a small tolerance of the expected value specified by FEM theory.

The second thing to notice is that, in any of these experiments, with a *fixed* element size one can always realize a comparable approximation with far fewer elements (giving enormous computational savings) by choosing b closer to a ($b = 1.2$ versus $b = 2$), see Figure 2. While this may, on the surface, seem to be obvious from the outset, it is noteworthy that the transparent boundary condition is unaffected by the complicated structure of the solution so near to the scattering surface.

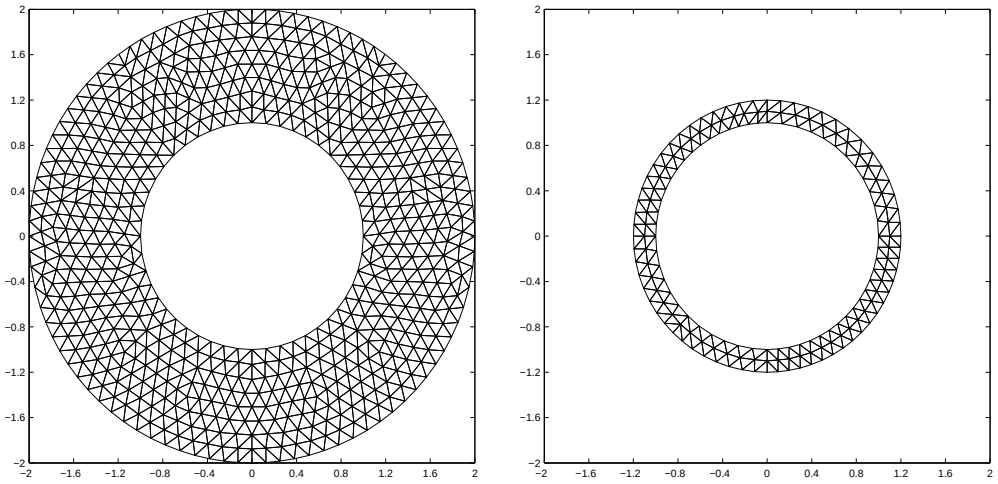

(a) $b = 2$ (b) $b = 1.2$

Fig. 2. Computational meshes at refinement level $h/h_1 = 1/2$ ($h_1 \approx 0.25$) for scattering from a circle with circular Artificial Boundaries. Left: $b = 2$. Right: $b = 1.2$.

5.2 Scattering from an Ellipse

We now consider a perfectly conducting scatterer shaped by an ellipse

$$x = a_1 \cos(\theta), \quad y = a_2 \sin(\theta),$$

Experiment	h/h_1	N_{el}	N_Γ	$N_\mathcal{B}$
CC(1)	1	302	24	46
CC(2)	1/2	1208	48	92
CC(3)	1/4	4832	96	184
CC(4)	1/8	19328	192	368
CC(5)	1/16	77312	384	736

Table 1
Mesh data for the circular scatterer ($a = 1$) with a circular artificial boundary ($b = 2$). $h_1 \approx 0.25$ and N_{el} is the number of elements in the mesh. N_Γ and $N_\mathcal{B}$ represent the number of points on the scatterer and artificial boundaries, respectively.

h/h_1	$k \approx 1$			$k \approx 10$		
	N_f	L^∞-error	ratio	N_f	L^∞-error	ratio
1	12	3.74e-03	–	32	1.63e+00	–
1/2	12	1.04e-03	1.85	32	8.13e-01	1.00
1/4	12	3.00e-04	1.79	32	2.01e-01	2.02
1/8	12	9.53e-05	1.65	32	5.22e-02	1.94
1/16	12	3.00e-05	1.67	32	1.33e-02	1.97

Table 2
Circular scatterer ($a = 1$) with a far circular artificial boundary ($b = 2$) and scheme order $p = 1$.

h/h_1	$k \approx 1$			$k \approx 10$		
	N_f	L^∞-error	ratio	N_f	L^∞-error	ratio
1	12	3.64e-04	–	36	2.72e-01	–
1/2	12	5.32e-05	2.78	36	2.41e-02	3.50
1/4	12	7.28e-06	2.87	36	2.12e-03	3.50
1/8	12	9.68e-07	2.91	36	2.13e-04	3.32
1/16	14	1.24e-07	2.96	36	2.28e-05	3.22

Table 3
Circular scatterer ($a = 1$) with a far circular artificial boundary ($b = 2$) and scheme order $p = 2$.

or, in polar coordinates,

$$r = a_1\sqrt{1 - e^2 \sin^2(\theta)},$$

h/h_1	$k \approx 1$			$k \approx 10$		
	N_f	L^∞-error	ratio	N_f	L^∞-error	ratio
1	16	3.85e-05	–	36	2.30e-02	–
1/2	16	2.95e-06	3.71	36	1.59e-03	3.85
1/4	16	2.46e-07	3.58	36	9.84e-05	4.02
1/8	16	1.96e-08	3.65	38	6.36e-06	3.95
1/16	20	1.37e-09	3.83	40	4.01e-07	3.99

Table 4
Circular scatterer ($a = 1$) with a far circular artificial boundary ($b = 2$) and scheme order $p = 3$.

h/h_1	$k \approx 1$			$k \approx 10$		
	N_f	L^∞-error	ratio	N_f	L^∞-error	ratio
1	16	3.12e-06	–	36	3.87e-03	–
1/2	16	1.38e-07	4.50	36	1.33e-04	4.86
1/4	18	4.79e-09	4.85	38	5.88e-06	4.50
1/8	18	1.63e-10	4.88	40	1.63e-07	5.18
1/16	20	5.29e-12	4.94	40	2.50e-08	2.70

Table 5
Circular scatterer ($a = 1$) with a far circular artificial boundary ($b = 2$) and scheme order $p = 4$.

Experiment	h/h_1	N_{el}	N_Γ	$N_\mathcal{B}$
CCC(1)	1	60	28	32
CCC(2)	1/2	240	56	64
CCC(3)	1/4	960	112	128
CCC(4)	1/8	3840	224	256
CCC(5)	1/16	15360	448	512

Table 6
Mesh data for the circular scatterer ($a = 1$) with a circular artificial boundary ($b = 1.2$). $h_1 \approx 0.25$ and N_{el} is the number of elements in the mesh. N_Γ and $N_\mathcal{B}$ represent the number of points on the scatterer and artificial boundaries, respectively.

where $e = \sqrt{1 - a_2^2/a_1^2}$ is the eccentricity. In this case

$$\Sigma_e = \left\{ r < a_1 \sqrt{1 - e^2 \sin^2(\theta)} \right\}, \quad \Gamma_e = \left\{ r = a_1 \sqrt{1 - e^2 \sin^2(\theta)} \right\}.$$

h/h_1	$k \approx 1$			$k \approx 10$		
	N_f	L^∞-error	ratio	N_f	L^∞-error	ratio
1	10	5.92e-03	–	28	4.90e-01	–
1/2	10	1.75e-03	1.76	28	1.47e-01	1.74
1/4	12	4.89e-04	1.84	30	4.29e-02	1.78
1/8	12	1.45e-04	1.76	32	1.36e-02	1.66
1/16	14	3.84e-05	1.91	32	3.88e-03	1.80

Table 7
Circular scatterer ($a = 1$) with a near circular artificial boundary ($b = 1.2$) and scheme order $p = 1$.

h/h_1	$k \approx 1$			$k \approx 10$		
	N_f	L^∞-error	ratio	N_f	L^∞-error	ratio
1	12	5.32e-04	–	30	1.11e-01	–
1/2	12	5.40e-05	3.30	32	1.11e-02	3.31
1/4	14	7.13e-06	2.92	34	1.60e-03	2.80
1/8	16	9.27e-07	2.94	36	1.98e-04	3.02
1/16	16	1.39e-07	2.74	38	2.97e-05	2.73

Table 8
Circular scatterer ($a = 1$) with a near circular artificial boundary ($b = 1.2$) and scheme order $p = 2$.

h/h_1	$k \approx 1$			$k \approx 10$		
	N_f	L^∞-error	ratio	N_f	L^∞-error	ratio
1	14	2.92e-05	–	34	1.35e-02	–
1/2	16	2.55e-06	3.51	36	1.19e-03	3.50
1/4	18	1.83e-07	3.81	38	8.50e-05	3.81
1/8	18	1.35e-08	3.76	42	5.18e-06	4.03
1/16	20	9.53e-10	3.82	44	3.80e-07	3.77

Table 9
Circular scatterer ($a = 1$) with a near circular artificial boundary ($b = 1.2$) and scheme order $p = 3$.

For this scatterer we display two sets of results, one where we enclose it with a circular artificial boundary,

$$\mathcal{B} = \{r = b_1\}$$

h/h_1	$k \approx 1$			$k \approx 10$		
	N_f	L^∞-error	ratio	N_f	L^∞-error	ratio
1	16	2.13e-06	–	38	2.40e-03	–
1/2	18	7.76e-08	4.78	40	1.01e-04	4.58
1/4	20	2.99e-09	4.70	44	3.17e-06	4.98
1/8	20	1.03e-10	4.86	46	1.04e-07	4.94
1/16	22	3.88e-12	4.73	50	3.29e-09	4.98

Table 10
Circular scatterer ($a = 1$) with a near circular artificial boundary ($b = 1.2$) and scheme order $p = 4$.

and a second where the ellipse is enclosed by another ellipse,

$$\mathcal{B} = \left\{ r = b_1 \sqrt{1 - \bar{e}^2 \sin^2(\theta)} \right\},$$

and $\bar{e} = \sqrt{1 - b_2^2/b_1^2}$; see Figure 3.

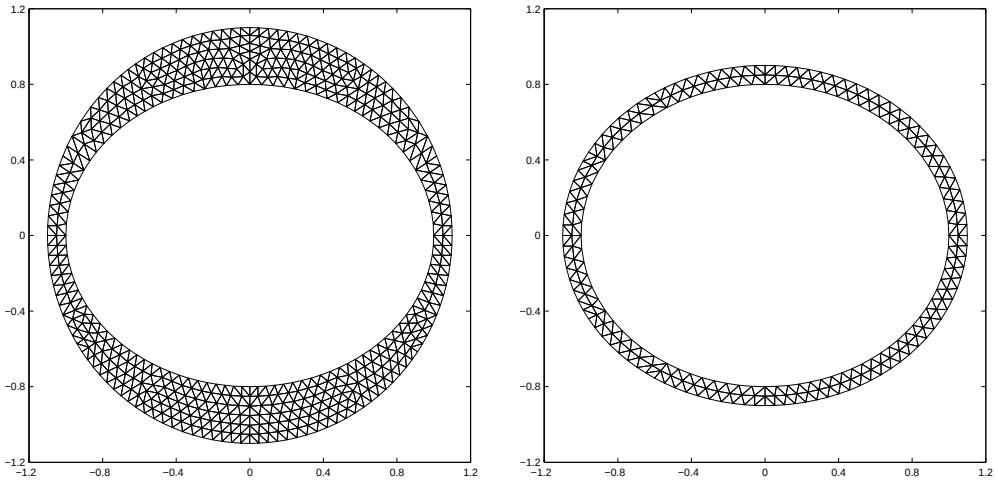

(a) Circular Artificial Boundary (b) Elliptical Artificial Boundary

Fig. 3. Computational meshes at refinement level $h/h_1 = 1/2$ ($h_1 \approx 0.25$) for scattering from an ellipse. Left: Circular Artificial Boundary. Right: Elliptical Artificial Boundary.

The numerical parameters for these experiments are listed in Tables 11 & 16, and we point out that, in the latter case, an exact boundary condition at the Artificial Boundary, $\mathcal{B}$, would require an infinite number of terms in the expansion of the DNO, (12). As we mentioned before, we approximate this infinite expansion with a truncated Taylor series, (13), where we have chosen

$N = 8$. An additional consideration in this case is how the partial sum (13) is to be computed. A strong case has been made in previous literature (see, e.g., [17,21,28,29]) for using Padé approximation [30] as it not only enhances convergence within the disk of analyticity of (12), but also allows for the summation of the series *outside* this disk. For the remainder of the experiments which require $N > 0$ (i.e., $\mathcal{B}$ non–circular) we use Padé summation. Finally, in all of the results presented in this section, save the last (Table 21), we have used the OE recursions. In this final simulation we use the FE formulas with Padé summation to show that the results are nearly identical (compare Table 19 with Table 21).

The results for the elliptical scatterer and circular artificial boundary are displayed in Tables 12–15, for polynomial orders $p = 1, 2, 3, 4$, respectively. Here, as there is no convenient exact solution, we measure the Cauchy convergence of our solution:

$$\text{ratio} := \text{ratio}(h_{n-2}, h_{n-1}, h_n) = \frac{\left| u_{h_{n-1}} - u_{h_{n-2}} \right|_{L^\infty}}{\left| u_{h_n} - u_{h_{n-1}} \right|_{L^\infty}};$$

note that we cannot compute this ratio for $n = 1, 2$. Again, we see (at least) the order of accuracy that we expect from each polynomial order and so conclude that the inclusion of the DtN–map has no effect on the performance of our underlying FEM.

Experiment	h/h_1	N_{el}	N_Γ	$N_\mathcal{B}$
EC(1)	1	234	52	62
EC(2)	1/2	936	104	124
EC(3)	1/4	3744	208	248
EC(4)	1/8	14976	416	496
EC(5)	1/16	59904	832	992

Table 11
Mesh data for the elliptical scatterer with $a_1 = 1, a_2 = 0.8$ and circular artificial boundary $b_1 = 1.1$. $h_1 \approx 0.25$ and N_{el} is the number of elements in the mesh. N_Γ and $N_\mathcal{B}$ represent the number of points on the scatterer and artificial boundaries, respectively.

The results for the elliptical scatterer and elliptical artificial boundary are displayed in Tables 17–20, for polynomial orders $p = 1, 2, 3, 4$, respectively. Again, the order of accuracy that one would expect from each polynomial order is realized, however, we point out that accuracies quite comparable to the circular Artificial Boundary can be realized with the elliptical $\mathcal{B}$ with the same element size but one half to one third the number of elements (see

h/h_1	$k \approx 1$			$k \approx 10$		
	N_f	L^∞-error	ratio	N_f	L^∞-error	ratio
1	4	–	–	24	–	–
1/2	4	5.42e-03	–	24	2.16e-01	–
1/4	4	1.68e-03	1.69	24	8.10e-02	1.42
1/8	4	4.05e-04	2.05	24	1.92e-02	2.08
1/16	4	1.13e-04	1.85	24	6.51e-03	1.56

Table 12
Elliptical scatterer $(a_1 = 1, a_2 = 0.8)$ with a circular artificial boundary $(b_1 = 1.1)$ and scheme order $p = 1$.

h/h_1	$k \approx 1$			$k \approx 10$		
	N_f	L^∞-error	ratio	N_f	L^∞-error	ratio
1	4	–	–	24	–	–
1/2	4	3.07e-04	–	24	4.77e-02	–
1/4	4	5.05e-05	2.60	24	6.25e-03	2.93
1/8	4	6.95e-06	2.86	24	8.59e-04	2.86
1/16	4	9.51e-07	2.87	24	1.03e-04	3.06

Table 13
Elliptical scatterer $(a_1 = 1, a_2 = 0.8)$ with a circular artificial boundary $(b_1 = 1.1)$ and scheme order $p = 2$.

h/h_1	$k \approx 1$			$k \approx 10$		
	N_f	L^∞-error	ratio	N_f	L^∞-error	ratio
1	4	–	–	24	–	–
1/2	4	1.48e-05	–	24	1.86e-03	–
1/4	4	1.38e-06	3.42	24	2.36e-04	2.98
1/8	4	8.62e-08	4.00	24	1.35e-05	4.13
1/16	4	6.23e-09	3.79	24	9.97e-07	3.76

Table 14
Elliptical scatterer $(a_1 = 1, a_2 = 0.8)$ with a circular artificial boundary $(b_1 = 1.1)$ and scheme order $p = 3$.

Tables 11 & 16). Again, we see the enormous computational savings that can be realized with our new approach.

To close, we revisit the experiment presented in Table 19, i.e. scattering from an ellipse enclosed by an elliptical Artificial Boundary with polynomial order

h/h_1	$k \approx 1$			$k \approx 10$		
	N_f	L^∞-error	ratio	N_f	L^∞-error	ratio
1	4	–	–	24	–	–
1/2	4	8.45e-07	–	24	5.26e-04	–
1/4	4	4.35e-08	4.28	24	1.58e-05	5.06
1/8	4	1.57e-09	4.79	24	5.54e-07	4.83
1/16	4	5.05e-11	4.96	24	1.69e-08	5.03

Table 15
Elliptical scatterer ($a_1 = 1, a_2 = 0.8$) with a circular artificial boundary ($b_1 = 1.1$) and scheme order $p = 4$.

Experiment	h/h_1	N_{el}	N_Γ	$N_\mathcal{B}$
EE(1)	1	94	43	51
EE(2)	1/2	376	86	102
EE(3)	1/4	1504	172	204
EE(4)	1/8	6016	344	408
EE(5)	1/16	24064	688	816

Table 16
Mesh data for the elliptical scatterer with $a_1 = 1.0, a_2 = 0.8$ and elliptical artificial boundary $b_1 = 1.1, b_2 = 0.9$. $h_1 \approx 0.25$ and N_{el} is the number of elements in the mesh. N_Γ and $N_\mathcal{B}$ represent the number of points on the scatterer and artificial boundaries, respectively.

h/h_1	$k \approx 1$			$k \approx 10$		
	N_f	L^∞-error	ratio	N_f	L^∞-error	ratio
1	14	–	–	26	–	–
1/2	14	4.06e-03	–	26	2.64e-01	–
1/4	14	1.07e-03	1.93	26	8.72e-02	1.60
1/8	14	2.98e-04	1.84	26	2.47e-02	1.82
1/16	14	7.06e-05	2.08	26	6.32e-03	1.97

Table 17
Elliptical scatterer ($a_1 = 1, a_2 = 0.8$) with an elliptical artificial boundary ($b_1 = 1.1, b_2 = 0.9$) and scheme order $p = 1$.

$p = 3$. However, we now choose to compute the terms T_n in the DNO via the FE algorithm. As we can see from Table 21, the results are identical up to the accuracy of our tables. Indeed, this has been our general experience and we can advocate the use of *either* OE or FE for these low–frequency applications.

h/h_1	$k \approx 1$			$k \approx 10$		
	N_f	L^∞-error	ratio	N_f	L^∞-error	ratio
1	14	–	–	26	–	–
1/2	14	2.90e-04	–	26	2.75e-02	–
1/4	14	4.47e-05	2.70	26	3.76e-03	2.87
1/8	14	6.66e-06	2.75	26	4.77e-04	2.98
1/16	14	8.55e-07	2.96	26	6.13e-05	2.96

Table 18
Elliptical scatterer ($a_1 = 1, a_2 = 0.8$) with an elliptical artificial boundary ($b_1 = 1.1, b_2 = 0.9$) and scheme order $p = 2$.

h/h_1	$k \approx 1$			$k \approx 10$		
	N_f	L^∞-error	ratio	N_f	L^∞-error	ratio
1	14	–	–	26	–	–
1/2	14	1.47e-05	–	26	3.28e-03	–
1/4	14	9.45e-07	3.96	26	2.45e-04	3.75
1/8	14	6.47e-08	3.87	26	1.29e-05	4.25
1/16	14	4.72e-09	3.78	26	8.56e-07	3.91

Table 19
Elliptical scatterer ($a_1 = 1, a_2 = 0.8$) with an elliptical artificial boundary ($b_1 = 1.1, b_2 = 0.9$) and scheme order $p = 3$.

h/h_1	$k \approx 1$			$k \approx 10$		
	N_f	L^∞-error	ratio	N_f	L^∞-error	ratio
1	14	–	–	26	–	–
1/2	14	1.39e-06	–	26	2.18e-04	–
1/4	14	1.85e-07	2.91	26	6.29e-06	5.11
1/8	14	1.83e-09	6.66	26	2.20e-07	4.84
1/16	14	2.32e-10	2.98	26	7.36e-09	4.90

Table 20
Elliptical scatterer ($a_1 = 1, a_2 = 0.8$) with an elliptical artificial boundary ($b_1 = 1.1, b_2 = 0.9$) and scheme order $p = 4$.

h/h_1	$k \approx 1$			$k \approx 10$		
	N_f	L^∞-error	ratio	N_f	L^∞-error	ratio
1	14	–	–	26	–	–
1/2	14	1.47e-05	–	26	3.28e-03	–
1/4	14	9.45e-07	3.96	26	2.45e-04	3.75
1/8	14	6.47e-08	3.87	26	1.29e-05	4.25
1/16	14	4.72e-09	3.78	26	8.56e-07	3.91

Table 21
Elliptical scatterer ($a_1 = 1, a_2 = 0.8$) with an elliptical artificial boundary ($b_1 = 1.1, b_2 = 0.9$) and scheme order $p = 3$. FE recursions are used to compute DNO terms T_n (c.f. Table 19).

5.3 Scattering from a Star–Shaped Obstacle

To conclude we consider a scatterer shaped by a perturbation of a circle of radius one

$$\Sigma_s = \{r < a + \delta\cos(4\theta)\}, \quad \Gamma_s = \{r = a + \delta\cos(4\theta)\}, \quad a = 1, \quad \delta = 0.4,$$

which we term "star–shaped." In our first set of experiments with this geometry we consider the DtN–FE method which encloses Σ_s with a circular artificial boundary

$$\mathcal{B} = \{r = b\}$$

where we have chosen $b = 1.5$; see Figure 4(a).

The numerical parameters for these simulations are given in Table 22, and the results of our experiments are summarized in Tables 23, 24, 25, & 26, for polynomial orders $p = 1, 2, 3, 4$, respectively. We note that the final refinements in Tables 25 & 26 are missing. This is due to the enormous size of these computations which necessitate the use of an iterative linear solver. With a desire to exclude the added considerations one must make for the convergence properties of such a scheme, and since these final data points are very unlikely to change our overall conclusions, we have omitted them.

Next, we consider our new method with an artificial boundary shaped to mimic that of the scatterer, i.e.

$$\mathcal{B} = \{r < b + \delta_b\cos(4\theta)\}, \quad b = 1.2, \quad \delta_b = 0.3;$$

see Figure 4(b). For this geometry, the numerical parameters are given in Table 27. As in the case of the elliptical Artificial Boundary in § 5.2, we must use the approximation (13) of the full DNO to enforce our boundary condition. For this we use $N = 8$, Padé summation, and the OE algorithm. The results with

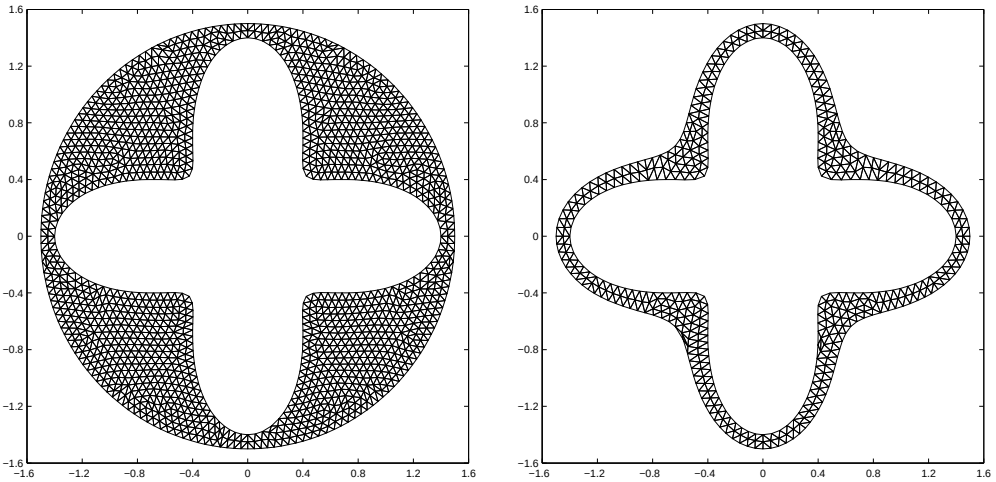

(a) Circular Artificial Boundary

(b) Star–Shaped Artificial Boundary

Fig. 4. Computational meshes at refinement level $h/h_1 = 1/2$ ($h_1 \approx 0.25$) for scattering from a star–shaped obstacle. Left: Circular Artificial Boundary. Right: Star–Shaped Artificial Boundary.

Experiment	h/h_1	N_{el}	N_Γ	$N_\mathcal{B}$
SC(1)	1	717	89	88
SC(2)	1/2	2868	178	176
SC(3)	1/4	11472	356	352
SC(4)	1/8	45888	712	704
SC(5)	1/16	183552	1424	1408

Table 22
Mesh data for the star–shaped scatterer ($a = 1$, $\delta = 0.4$) with a circular artificial boundary ($b = 1.5$). $h_1 \approx 0.25$ and N_{el} is the number of elements in the mesh. N_Γ and $N_\mathcal{B}$ represent the number of points on the scatterer and artificial boundaries, respectively.

this star–shaped Artificial Boundary are summarized in Tables 28, 29, 30, & 31, for polynomial orders $p = 1, 2, 3, 4$, respectively. We again notice the negligible impact that our Enhanced DtN–FE algorithm has on the convergence of the underlying FEM.

An inspection of Tables 23–26 and Tables 28–31 once again indicates that the transparent boundary condition has *no* affect on the rate of convergence of the FEM, for any order of convergence. In these simulations the numerical parameters were chosen so that, at corresponding polynomial orders, the star/circle and star/star configurations would realize comparable errors (this is clearly visible from comparisons of Table 23 with Table 28, etc.). However, an inspec-

h/h_1	$k \approx 1$			$k \approx 10$		
	N_f	L^∞-error	ratio	N_f	L^∞-error	ratio
1	4	–	–	32	–	–
1/2	4	9.57e-03	–	32	3.47e-01	–
1/4	4	2.10e-03	2.19	32	1.14e-01	1.61
1/8	4	5.74e-04	1.87	32	2.97e-02	1.94
1/16	4	1.44e-04	1.99	32	7.30e-03	2.02

Table 23
Star–shaped scatterer ($a = 1$, $\delta = 0.4$) with a circular artificial boundary ($b = 1.5$) and scheme order $p = 1$.

h/h_1	$k \approx 1$			$k \approx 10$		
	N_f	L^∞-error	ratio	N_f	L^∞-error	ratio
1	4	–	–	32	–	–
1/2	4	5.66e-04	–	32	2.25e-02	–
1/4	4	9.59e-05	2.56	32	2.86e-03	2.98
1/8	4	1.36e-05	2.82	32	3.53e-04	3.02
1/16	4	1.90e-06	2.84	32	4.29e-05	3.04

Table 24
Star–shaped scatterer ($a = 1$, $\delta = 0.4$) with a circular artificial boundary ($b = 1.5$) and scheme order $p = 2$.

h/h_1	$k \approx 1$			$k \approx 10$		
	N_f	L^∞-error	ratio	N_f	L^∞-error	ratio
1	4	–	–	32	–	–
1/2	4	5.65e-05	–	32	2.18e-03	–
1/4	4	4.52e-06	3.64	32	1.61e-04	3.76
1/8	4	2.32e-07	4.29	32	1.01e-05	4.00

Table 25
Star–shaped scatterer ($a = 1$, $\delta = 0.4$) with a circular artificial boundary ($b = 1.5$) and scheme order $p = 3$.

tion of these parameters, provided in Tables 22 & 27, reveals that this can be accomplished with far fewer elements in the star/star case, typically by a factor of almost four.

h/h_1	$k \approx 1$			$k \approx 10$		
	N_f	L^∞-error	ratio	N_f	L^∞-error	ratio
1	4	–	–	32	–	–
1/2	4	4.44e-06	–	32	2.26e-04	–
1/4	4	2.59e-07	4.10	32	1.01e-05	4.48
1/8	4	7.33e-09	5.15	32	2.87e-07	5.14

Table 26
Star–shaped scatterer ($a = 1$, $\delta = 0.4$) with a circular artificial boundary ($b = 1.5$) and scheme order $p = 4$.

Experiment	h/h_1	N_{el}	N_Γ	$N_\mathcal{B}$
SS(1)	1	189	78	75
SS(2)	1/2	756	156	150
SS(3)	1/4	3024	312	300
SS(4)	1/8	12096	624	600
SS(5)	1/16	48384	1248	1200

Table 27
Mesh data for the star–shaped scatterer ($a = 1$, $\delta = 0.4$) with a star–shaped artificial boundary ($a = 1.2$, $\delta_b = 0.3$). $h_1 \approx 0.25$ and N_{el} is the number of elements in the mesh. N_Γ and $N_\mathcal{B}$ represent the number of points on the scatterer and artificial boundaries, respectively.

h/h_1	$k \approx 1$			$k \approx 10$		
	N_f	L^∞-error	ratio	N_f	L^∞-error	ratio
1	60	–	–	84	–	–
1/2	60	1.12e-02	–	84	4.18e-01	–
1/4	60	3.27e-03	1.78	84	1.10e-01	1.92
1/8	60	8.82e-04	1.89	84	3.19e-02	1.79
1/16	60	2.31e-04	1.93	84	8.09e-03	1.98

Table 28
Star–shaped scatterer ($a = 1$, $\delta = 0.4$) with a star–shaped artificial boundary ($b = 1.2$, $\delta_b = 0.3$) and scheme order $p = 1$.

6 Conclusions

In this paper we have demonstrated not only how the DtN–FE method can be correctly combined with a high–order *hp*–FEM to yield numerical results which do not degrade the performance of the underlying FEM, but also how the

h/h_1	$k \approx 1$			$k \approx 10$		
	N_f	L^∞-error	ratio	N_f	L^∞-error	ratio
1	60	–	–	84	–	–
1/2	60	1.74e-03	–	84	3.37e-02	–
1/4	60	2.64e-04	2.72	84	4.55e-03	2.89
1/8	60	4.22e-05	2.65	84	5.40e-04	3.07
1/16	60	4.86e-06	3.12	84	7.23e-05	2.90

Table 29
Star–shaped scatterer ($a = 1$, $\delta = 0.4$) with a circular artificial boundary ($b = 1.6$) and scheme order $p = 2$.

h/h_1	$k \approx 1$			$k \approx 10$		
	N_f	L^∞-error	ratio	N_f	L^∞-error	ratio
1	60	–	–	84	–	–
1/2	60	1.81e-04	–	84	3.58e-03	–
1/4	60	1.36e-05	3.73	84	2.30e-04	3.96
1/8	60	8.66e-07	3.98	84	1.64e-05	3.81
1/16	60	5.54e-08	3.97	84	8.98e-07	4.19

Table 30
Star–shaped scatterer ($a = 1$, $\delta = 0.4$) with a star–shaped artificial boundary ($b = 1.2$, $\delta_b = 0.3$) and scheme order $p = 3$.

h/h_1	$k \approx 1$			$k \approx 10$		
	N_f	L^∞-error	ratio	N_f	L^∞-error	ratio
1	60	–	–	88	–	–
1/2	60	2.19e-05	–	88	4.11e-04	–
1/4	60	1.21e-06	4.18	88	1.94e-05	4.41
1/8	60	3.50e-08	5.11	88	6.57e-07	4.88
1/16	60	1.18e-09	4.90	88	2.05e-08	5.01

Table 31
Star–shaped scatterer ($a = 1$, $\delta = 0.4$) with a star–shaped artificial boundary ($b = 1.2$, $\delta_b = 0.3$) and scheme order $p = 4$.

fundamental Artificial Boundary shape requirement can be relaxed to allow for quite general shapes. This "Enhanced DtN–FE Method" has been shown to be quite robust and flexible, and, with a suitably chosen Artificial Boundary, can deliver accurate answers with one half to one quarter the number of finite elements required by the DtN–FE method.

A Adjointness of the Dirichlet–to–Neumann Map

In this appendix we describe the adjointness properties of the DtN map, T, which enable its rapid evaluation in the "Operator Expansions" (OE) methodology (see § 4.2). To begin, let us study the adjointness of Fourier multipliers with the following Lemma.

Lemma 1 *If the Fourier multiplier $m(D)$ has symbol $m(p)$ then its adjoint $n(D) := m^*(D)$ has symbol $n(p) = \overline{m(p)}$.*

PROOF. We begin by recalling that the L^2–inner product for complex–valued, 2π–periodic functions ξ and ψ satisfies

$$\begin{aligned}\langle \xi, \psi \rangle &= \int_0^{2\pi} \xi(\theta)\overline{\psi(\theta)}\, d\theta = \int_0^{2\pi} \left(\sum_{p=-\infty}^{\infty} \hat{\xi}_p e^{ip\theta} \right) \overline{\left(\sum_{p=-\infty}^{\infty} \hat{\psi}_p e^{ip\theta} \right)}\, d\theta \\ &= \sum_{p=-\infty}^{\infty} \sum_{q=-\infty}^{\infty} \hat{\xi}_p \overline{\hat{\psi}_q} \int_0^{2\pi} e^{i(p-q)\theta}\, d\theta = 2\pi \sum_{p=-\infty}^{\infty} \hat{\xi}_p \overline{\hat{\psi}_p}.\end{aligned}$$

With this calculation in mind we can now compute:

$$\begin{aligned}\langle m(D)\xi, \psi \rangle &= 2\pi \sum_{p=-\infty}^{\infty} m(p)\hat{\xi}_p\, \overline{\hat{\psi}_p} = 2\pi \sum_{p=-\infty}^{\infty} \hat{\xi}_p\, \overline{\overline{m(p)}\hat{\psi}_p} \\ &= 2\pi \sum_{p=-\infty}^{\infty} \hat{\xi}_p\, \overline{n(p)\hat{\psi}_p} = \langle \xi, n(D)\psi \rangle\,,\end{aligned}$$

so that $m^* = n$ where $n(p) = \overline{m(p)}$.

With Lemma 1 in mind it is easy to show that, for the DtN map in the simple case of zero boundary perturbation, i.e.

$$T_0[\psi] = -kb \frac{d_z H_D^{(1)}(kb)}{H_D^{(1)}(kb)}[\psi],$$

c.f. (10), the adjoint is

$$T_0^* = \overline{-kb \frac{d_z H_D^{(1)}(kb)}{H_D^{(1)}(kb)}} = -kb \frac{d_z H_D^{(2)}(kb)}{H_D^{(2)}(kb)} =: S_0.$$

Of course, $S_0^* = T_0$ as well, a fact that we will use later.

The goal of this section is to find a *rapid* OE formula for the evaluation of the DNO. In the case of solving Laplace's equation ($k = 0$ in (2)) one can

take advantage of the fact that the DNO is *self–adjoint* to take the adjoint of (19) and reverse the order of the operators. At first this would not appear to accelerate the procedure, but a careful inspection of (19) reveals that if the operator T_l were applied to the *same* function ψ at every order (rather than different ones) then these could be saved from one order to the next, resulting in an algorithm with the same computational complexity as the FE algorithm.

Of course $S_0 \neq T_0$ for $k \neq 0$ so this idea will not work directly for the DNO associated to the Helmholtz equation. However, a modification of this idea will produce a fast algorithm. If S is the adjoint of T then, of course, T is the adjoint of S. If we can find an algorithm analogous to (19) for S, then we could take the adjoint of S_n (reversing the order of the operators) to find a *fast* algorithm for T_n. With this in mind we now have three tasks: Find the problem for S, find the OE method for S, and conjugate this OE method.

For the first let us consider (7) & (8) and identify the adjoint of T. To begin, define *another* transparent boundary at $r = c$ which is exterior to $\mathcal{B}$. Following the development of § 2.1 it is easy to see that (7) can be equivalently stated as

$$\Delta w + k^2 w = 0 \qquad \text{in } \mathcal{A}_{\mathcal{B},c} := \mathrm{Ext}(\mathcal{B}) \cap \{r < c\} \tag{A.1a}$$
$$w = \psi \qquad \text{at } \mathcal{B} \tag{A.1b}$$
$$\partial_r w - Jw = 0 \qquad \text{at } r = c, \tag{A.1c}$$

where

$$J := ck \frac{d_z H_D^{(1)}(kc)}{H_D^{(1)}(kc)}.$$

Note the opposite sign of J as compared to T since the outward direction is now the *positive* radial direction. We propose the "adjoint problem"

$$\Delta u + k^2 u = 0 \qquad \text{in } \mathcal{A}_{\mathcal{B},c} \tag{A.2a}$$
$$u = \eta \qquad \text{at } \mathcal{B} \tag{A.2b}$$
$$\partial_r u - Ku = 0 \qquad \text{at } r = c, \tag{A.2c}$$

where K is to be determined, which defines the "adjoint" of the DNO, T,

$$S[\eta] := \nabla u|_{\mathcal{B}} \cdot N. \tag{A.3}$$

We will now make the notion of (A.2)–(A.3) as adjoint of (7)–(8) more precise. We begin with the calculation

$$\langle T[\psi], \eta \rangle = \int_0^{2\pi} T[\psi] \overline{\eta}\, d\theta = \int_0^{2\pi} (\partial_n w)\, |N|\, \overline{u}\, d\theta = \int_{\mathcal{B}} (\partial_n w) \overline{u}\, ds,$$

where n is the *unit* normal. It is here that we see how the particular choice of normal, N, is crucial to our adjointness arguments. Continuing via the

divergence theorem (applied to the bounded domain $\mathcal{A}_{\mathcal{B},c}$):

$$\begin{aligned}\langle T[\psi],\eta\rangle &= \int_{\mathcal{A}_{\mathcal{B},c}} \operatorname{div}\left[\nabla w\overline{u}\right]\, dV - \int_{r=c}(\partial_r w)\overline{u}\, ds \\ &= \int_{\mathcal{A}_{\mathcal{B},c}} \Delta w\overline{u}\, dV + \int_{\mathcal{A}_{\mathcal{B},c}} \nabla w\cdot\overline{\nabla u}\, dV - \int_{r=c}(\partial_r w)\overline{u}\, ds \\ &= \int_{\mathcal{A}_{\mathcal{B},c}} -k^2 w\overline{u}\, dV + \int_{\mathcal{A}_{\mathcal{B},c}} \operatorname{div}\left[w\overline{\nabla u}\right]\, dV \\ &\quad - \int_{\mathcal{A}_{\mathcal{B},c}} w\overline{\Delta u}\, dV - \int_{r=c}(\partial_r w)\overline{u}\, ds,\end{aligned}$$

where we have used the fact that w satisfies the Helmholtz equation. Using the reality of k, the fact that u satisfies the Helmholtz equation, and, again, the divergence theorem:

$$\begin{aligned}\langle T[\psi],\eta\rangle = &\int_{\mathcal{A}_{\mathcal{B},c}} -k^2 w\overline{u}\, dV + \int_{\mathcal{B}} w\overline{\partial_n u}\, ds + \int_{r=c} w\overline{\partial_r u}\, dV \\ &- \int_{\mathcal{A}_{\mathcal{B},c}} w(-k^2)\overline{u}\, dV - \int_{r=c}(\partial_r w)\overline{u}\, ds.\end{aligned}$$

The first and fourth term cancel leaving:

$$\langle T[\psi],\eta\rangle = \langle \psi, S[\eta]\rangle + \left\langle w|_{r=c}, K[u|_{r=c}]\right\rangle - \left\langle J[w|_{r=c}], u|_{r=c}\right\rangle.$$

Clearly, S is the adjoint of T provided that K is the adjoint of J which implies

$$K := ck\frac{d_z H_D^{(2)}(kc)}{H_D^{(2)}(kc)},$$

from Lemma 1.

Following the development of § 4.2 it is easy to find OE recursions for the *adjoint* operator S. We begin with

$$u_p(r,\theta) = H_p^{(2)}(kr)e^{ip\theta},$$

which satisfies the Helmholtz equation and the condition at $r=c$, and insert this into the definition of S yielding

$$\begin{aligned}S(\varepsilon f)\left[H_p^{(2)}(k(b+\varepsilon f))e^{ip\theta}\right] = &-(b+\varepsilon f)\partial_r\left(H_p^{(2)}(kr)e^{ip\theta}\right)\Big|_{r=b+\varepsilon f} \\ &+ \frac{\varepsilon\partial_\theta f}{b+\varepsilon f}\partial_\theta\left(H_p^{(2)}(kr)e^{ip\theta}\right)\Big|_{r=b+\varepsilon f}.\end{aligned}$$

For the expansion $S(\varepsilon f) = \sum_{n=0}^{\infty} S_n(f)\varepsilon^n$, we have

$$S_0[\eta] = -bk\frac{d_z H_D^{(2)}(kb)}{H_D^{(2)}(kb)}[\eta], \tag{A.4}$$

and, using $\partial_\theta^* = -\partial_\theta$,

$$\begin{aligned} S_n(f)[\eta] = &-bkC_n \frac{d_z^{n+1} H_D^{(2)}(kb)}{H_D^{(2)}(kb)}[\eta] - kfC_{n-1}\frac{d_z^n H_D^{(2)}(kb)}{H_D^{(2)}(kb)}[\eta] \\ &+ \sum_{l=0}^{n-1} C_{n-1-l}\frac{(\partial_\theta f)(-1)^l f^l}{b^{l+1}}\partial_\theta \frac{d_z^{n-1-l} H_D^{(2)}(kb)}{H_D^{(2)}(kb)}[\eta] \\ &- \sum_{l=0}^{n-1} S_l(f)\left[C_{n-l}\frac{d_z^{n-l} H_D^{(2)}(kb)}{H_D^{(2)}(kb)}[\eta]\right]. \end{aligned} \tag{A.5}$$

Defining

$$M_n(D) := \frac{d_z^n H_D^{(2)}(kb)}{H_D^{(2)}(kb)},$$

and taking the adjoint, we find

$$S_0^*[\eta] = -bk\frac{d_z H_D^{(1)}(kb)}{H_D^{(1)}(kb)}[\eta] = T_0[\eta], \tag{A.6}$$

and

$$\begin{aligned} S_n^*(f)[\eta] = &-bkM_{n+1}^*[C_n\eta] - kM_n^*[fC_{n-1}\eta] \\ &- \sum_{l=0}^{n-1} M_{n-1-l}^*\partial_\theta\left[C_{n-1-l}\frac{(\partial_\theta f)(-1)^l f^l}{b^{l+1}}\eta\right] \\ &- \sum_{l=0}^{n-1} M_{n-l}^*\left[C_{n-l}S_l^*(f)[\eta]\right], \end{aligned}$$

Since $S_n^* = T_n$ and

$$M_n^* = \frac{d_z^n H_D^{(1)}(kb)}{H_D^{(1)}(kb)},$$

this provides a rapid formula for the computation of the T_n:

$$\begin{aligned} T_n(f)[\psi] = &-bk\frac{d_z^{n+1} H_D^{(1)}(kb)}{H_D^{(1)}(kb)}[C_n\psi] - k\frac{d_z^n H_D^{(1)}(kb)}{H_D^{(1)}(kb)}[fC_{n-1}\psi] \\ &- \sum_{l=0}^{n-1}\frac{d_z^{n-1-l} H_D^{(1)}(kb)}{H_D^{(1)}(kb)}\partial_\theta\left[C_{n-1-l}\frac{(\partial_\theta f)(-1)^l f^l}{b^{l+1}}\psi\right] \\ &- \sum_{l=0}^{n-1}\frac{d_z^{n-l} H_D^{(1)}(kb)}{H_D^{(1)}(kb)}\left[C_{n-l}T_l(f)[\psi]\right], \end{aligned}$$

as the operators T_l are now applied solely to the function ψ and may be stored at every order.

Acknowledgements

DPN gratefully acknowledges support from the NSF through grant No. DMS–0537511.

References

[1] D. Colton, R. Kress, Inverse acoustic and electromagnetic scattering theory, 2nd Edition, Springer-Verlag, Berlin, 1998.

[2] F. Ihlenburg, Finite element analysis of acoustic scattering, Springer-Verlag, New York, 1998.

[3] K. Feng, Finite element method and natural boundary reduction, in: Proceedings of the International Congress of Mathematicians, Vol. 1, 2 (Warsaw, 1983), PWN, Warsaw, 1984, pp. 1439–1453.

[4] H. D. Han, X. N. Wu, Approximation of infinite boundary condition and its application to finite element methods, J. Comput. Math. 3 (2) (1985) 179–192.

[5] J. B. Keller, D. Givoli, Exact nonreflecting boundary conditions, J. Comput. Phys. 82 (1) (1989) 172–192.

[6] D. Givoli, Nonreflecting boundary conditions, J. Comput. Phys. 94 (1) (1991) 1–29.

[7] D. Givoli, J. B. Keller, Special finite elements for use with high-order boundary conditions, Comput. Methods Appl. Mech. Engrg. 119 (3-4) (1994) 199–213.

[8] D. Givoli, Numerical methods for problems in infinite domains, Vol. 33 of Studies in Applied Mechanics, Elsevier Scientific Publishing Co., Amsterdam, 1992.

[9] D. Givoli, Recent advances in the DtN FE method, Arch. Comput. Methods Engrg. 6 (2) (1999) 71–116.

[10] D. P. Nicholls, N. Nigam, Exact non-reflecting boundary conditions on general domains, J. Comput. Phys. 194 (1) (2004) 278–303.

[11] D. P. Nicholls, N. Nigam, Error analysis of a coupled finite element/DtN map algorithm on general domains, Numer. Math. 105 (2) (2006) 267–298.

[12] M. Dubiner, Spectral methods on triangles and other domains, SIAM J. Sci. Comput. 6 (4) (1991) 345–390.

[13] T. C. Warburton, S. J. Sherwin, G. E. Karniadakis, Basis functions for triangular and quadrilateral high-order elements, SIAM J. Sci. Comput. 20 (5) (1999) 1671–1695 (electronic).

[14] L. Rayleigh, On the dynamical theory of gratings, Proc. Roy. Soc. London A79 (1907) 399–416.

[15] S. O. Rice, Reflection of electromagnetic waves from slightly rough surfaces, Comm. Pure Appl. Math. 4 (1951) 351–378.

[16] O. P. Bruno, F. Reitich, Numerical solution of diffraction problems: A method of variation of boundaries, J. Opt. Soc. Am. A 10 (6) (1993) 1168–1175.

[17] O. P. Bruno, F. Reitich, Numerical solution of diffraction problems: A method of variation of boundaries. II. Finitely conducting gratings, Padé approximants, and singularities, J. Opt. Soc. Am. A 10 (11) (1993) 2307–2316.

[18] O. P. Bruno, F. Reitich, Numerical solution of diffraction problems: A method of variation of boundaries. III. Doubly periodic gratings, J. Opt. Soc. Am. A 10 (12) (1993) 2551–2562.

[19] O. P. Bruno, F. Reitich, Calculation of electromagnetic scattering via boundary variations and analytic continuation, Appl. Comput. Electromagn. Soc. J. 11 (1) (1996) 17–31.

[20] O. P. Bruno, F. Reitich, Boundary–variation solutions for bounded–obstacle scattering problems in three dimensions, J. Acoust. Soc. Am. 104 (5) (1998) 2579–2583.

[21] O. P. Bruno, F. Reitich, High-order boundary perturbation methods, in: Mathematical Modeling in Optical Science, Vol. 22, SIAM, Philadelphia, PA, 2001, pp. 71–109, frontiers in Applied Mathematics Series.

[22] D. M. Milder, An improved formalism for rough-surface scattering of acoustic and electromagnetic waves, in: Proceedings of SPIE - The International Society for Optical Engineering (San Diego, 1991), Vol. 1558, Int. Soc. for Optical Engineering, Bellingham, WA, 1991, pp. 213–221.

[23] D. M. Milder, An improved formalism for wave scattering from rough surfaces, J. Acoust. Soc. Am. 89 (2) (1991) 529–541.

[24] D. M. Milder, H. T. Sharp, Efficient computation of rough surface scattering, in: Mathematical and numerical aspects of wave propagation phenomena (Strasbourg, 1991), SIAM, Philadelphia, PA, 1991, pp. 314–322.

[25] D. M. Milder, H. T. Sharp, An improved formalism for rough surface scattering. ii: Numerical trials in three dimensions, J. Acoust. Soc. Am. 91 (5) (1992) 2620–2626.

[26] D. M. Milder, Role of the admittance operator in rough-surface scattering, J. Acoust. Soc. Am. 100 (2) (1996) 759–768.

[27] D. M. Milder, An improved formalism for electromagnetic scattering from a perfectly conducting rough surface, Radio Science 31 (6) (1996) 1369–1376.

[28] D. P. Nicholls, F. Reitich, Stability of high-order perturbative methods for the computation of Dirichlet-Neumann operators, J. Comput. Phys. 170 (1) (2001) 276–298.

[29] D. P. Nicholls, F. Reitich, Shape deformations in rough surface scattering: Improved algorithms, J. Opt. Soc. Am. A 21 (4) (2004) 606–621.

[30] G. A. Baker, Jr., P. Graves-Morris, Padé approximants, 2nd Edition, Cambridge University Press, Cambridge, 1996.